May 2019

Haro 11, Pox 186, and VCC 1313: The Enigmatic Behavior of HI Non-Emitters

Sarah H. Taft

Macalester College, staft@macalester.edu

Abstract

We present neutral hydrogen (HI) observations from the Very Large Array (VLA) telescope of the galaxies Haro 11, Pox 186, and VCC 1313. 24 hours of deep spectral line observation at the 21 cm line were obtained from the program 17B-287 of Haro 11, the primary galaxy studied in this capstone, and 176 and 203 respective minutes of archival VLA data at the 21 cm line were obtained from the program AS0832 of Pox 186 and VCC 1313, the secondary and tertiary sources of study for this capstone. Haro 11 is one of a very small number of local dwarf galaxies to be both a Lyα and LyC emitter. While it harbors ongoing aggressive star formation (with sources reporting up to 32.8 $M_\odot$ yr^{-1}), the neutral hydrogen gas in the system has been notoriously difficult to detect. Previous interferometric observations have resulted in non-detections, while a deep Green Bank Telescope (GBT) spectrum reveals a weak spectral line. Our emission result is a non-detection, while our absorption result is a detection, confirming the results of similar, previously conducted absorption work. Past interferometric research has additionally resulted in HI non-detections for both Pox 186 and VCC 1313. Our results from archival data are also two HI non-detections, confirming the results of past research. For all three systems, given their aggressive star formation rates, these HI non-detection results are surprising. The behavior of these systems remains highly enigmatic.

Follow this and additional works at: https://digitalcommons.macalester.edu/mjpa

Part of the Astrophysics and Astronomy Commons, and the Physics Commons

Footer Logo

HARO 11, POX 186, AND VCC 1313: THE ENIGMATIC BEHAVIOR OF HI NON-EMITTERS

Sarah H. Taft

Department of Physics & Astronomy, Macalester College

Abstract

We present neutral hydrogen (HI) observations from the Very Large Array (VLA) telescope of the galaxies Haro 11, Pox 186, and VCC 1313. 24 hours of deep spectral line observation at the 21 cm line were obtained from the program 17B-287 of Haro 11, the primary galaxy studied in this capstone, and 176 and 203 respective minutes of archival VLA data at the 21 cm line were obtained from the program AS0832 of Pox 186 and VCC 1313, the secondary and tertiary sources of study for this capstone. Haro 11 is one of a very small number of local dwarf galaxies to be both a Lyα and LyC emitter. While it harbors ongoing aggressive star formation (with sources reporting up to 32.8 M$_\odot$ yr^{-1}), the neutral hydrogen gas in the system has been notoriously difficult to detect. Previous interferometric observations have resulted in non-detections, while a deep Green Bank Telescope (GBT) spectrum reveals a weak spectral line. Our emission result is a non-detection, while our absorption result is a detection, confirming the results of similar, previously conducted absorption work. Past interferometric research has additionally resulted in HI non-detections for both Pox 186 and VCC 1313. Our results from archival data are also two HI non-detections, confirming the results of

2

past research. For all three systems, given their aggressive star formation rates, these HI non-detection results are surprising. The behavior of these systems remains highly enigmatic.

1. INTRODUCTION

Galactic morphology, kinematics, and gravitational interaction are among the most important subjects studied in the broader field of astrophysics. While there exist many tools to conduct these types of study, one of the most significant is the 21 cm line. Neutral hydrogen gas, a prominent component of galaxies, especially star forming ones, can be observed at this line (λ = 21 cm), a wavelength existing in the radio region of the electromagnetic spectrum. Emission at the 21 cm line arises from a spin flip transition in a hydrogen atom's electron. When the spin of the electron flips from one of a higher energy state, and parallel to the spin of the atom's nuclear magneton, to one of a lower energy state, and antiparallel to the spin of the nuclear magneton, a photon is emitted, assuming this transition is not due to a collision. This transition has been heavily studied, meaning the photon's energy is known to a high degree of accuracy, and corresponds to the aforementioned wavelength of 21 cm and frequency of 1420 MHz (Field 1959). Although this transition is a powerful one, it occurs very infrequently. Once the alignment of the electron is spin parallel, several million years may elapse before the spin flips to antiparallel and a photon is emitted. Despite this, observing HI is possible due to hydrogen's universal abundance.

Studying this line is intriguing for a number of reasons, including its ability to penetrate dust, gasses, and other material found in the interstellar medium (ISM) of galaxies, allowing star formation, galactic kinematics, and redshift to be mapped with clarity often not possible at other wavelengths. Past research conducted by Teich et al. (2016) has also found a correlation between HI mass and UV-based star formation rates (SFRs) in dwarf galaxies similar to the three explored in this work.

As HI column density increases, the authors found, the correlation between HI mass and UV-based SFR increases. This is significant for this capstone as all three sources possess high SFRs, making studying these galaxies at the 21 cm line furthermore intriguing.

Another tool used to study galactic behavior is the Lyα line. With a wavelength of $\lambda = 1216$ Å, Lyα emission arises from the de-excitation of a photoexcited electron in a neutral hydrogen atom from the quantum n=2 state to the n=1 state. The Lyα line is astrophysically significant due to its theorized contribution to the reionization of the early universe (Ouchi et al. 2009), as well as its ability to act as a star formation probe to otherwise unreachable galaxies at great redshifts (Cowie & Hu 1998). When a Lyα photon comes into contact with HI atoms at rest velocity, it undergoes a process called resonant scattering. This means that the Lyα photon is absorbed by the HI atom upon contact, and re-emitted in a different direction, resulting in complicated radiative transfer of Lyα emission. On a galactic scale, there are multiple factors thought to contribute to this resonant scattering process, including dust content and morphology (Hayes et al. 2010), and neutral gas content and kinematics (Cannon et al. 2004), especially of neutral hydrogen.

At the intersection of Lyα and HI observation lies the Luminous Compact Blue Galaxy (LCBG) Haro 11, an optical HST image of which can be seen in Figure 1. LCBGs are rare in the local universe (i.e. $z \leq 3$), and are defined as being prominently blue in color, high in both luminosity and surface brightness (i.e. M$_B$ < -18.5, Garland et al. 2004), rich in gas, and most likely the result of past mergers (Östlin et al. 2001). In addition to being an LCBG, Haro 11 is both a Lyα line (Hayes et al. 2007) and LyC (Bergvall et al. 2006; Bergvall et al. 2013; Leitet et al. 2013; Leitherer et al. 2016) emitter, one of a small number of local dwarfs to exhibit such emission. The source of this Lyα and LyC emission is highly contested, but past research conducted on Haro 11's star formation knots suggest these knots as potential Lyα emission sources. Two of these star formation knots, knots A and B, exhibit Lyα absorption, while knot C exhibits Lyα emission, an odd phenomenon given the

4

conclusion by Atek et al. (2008) that the respective dust content and extinction values of knots B and C are very similar. Nonetheless, it is thought that knot C is one of the primary contributors to Haro 11's Lyα emission. A Lyα image of Haro 11 can be seen in Figure 2.

Haro 11 also possesses a number of other noteworthy characteristics. Previous Hα observations have produced upper limits on the SFR of Haro 11 from 24 M$_\odot$ yr^{-1} (Hayes et al. 2007) up to 32.8 M$_\odot$ yr^{-1} (MacHattie et al. 2014). Its metallicity is also low, with a value of Z/Z$_\odot$ = $10^{8.2}/10^{8.69}$ (Guseva et al. 2012). In spite of its high star formation rate and complex Lyα radiative transfer, the HI content of Haro 11 has been highly confounding and remains so to this day. A search through archival VLA observations led to the first absorption detection of HI in Haro 11 by MacHattie et al. (2014). This detection led to further HI research on Haro 11, and eventually to an emission detection by Pardy et al. (2016) using single-dish GBT data. This 8σ detection, however, contained some inherent uncertainty, most notably the shift in the center of the spectral line redward of the system's optical velocity. This is where the interferometric VLA observations of Haro 11 at the 21 cm line, the primary data upon which this capstone is based, become significant. The goal of this program was to confirm or refute the HI emission detection made by Pardy et al. (2016), and if confirmed, map the kinematics of the gas in an attempt to unravel Haro 11's complex behavior. Since the result of this program is an HI emission non-detection, the kinematics and morphology of the galaxy are not mapped, and the HI properties of Haro 11 remain enigmatic.

Secondary and tertiary galaxies, Pox 186 and VCC 1313 respectively, are also studied in this capstone, and serve as smaller, dimmer analogs to Haro 11. Optical images of both galaxies can be seen in Figures 3 and 4. Both are classified as Blue Compact Dwarfs (BCDs). Though the precise criteria for classification as a BCD are still debated to this day, according to Thuan & Martin (1981), BCDs must possess a bolometric luminosity of M$_B$ $\leq$ -18 mag, an optical diameter of d$_{OPT}$ < 1 kpc, and intense and narrow optical emission lines, similar to those seen in the HII regions of spiral

galaxies. Additional research also suggests that many BCDs possess older stellar populations, with ages of at least a few 10^9 yrs (Amorìn et al. 2007), and that the star formation in a high percentage of BCDs is triggered by galaxy merging (Östlin et al. 2001). In addition to this classification, both galaxies possess a number of noteworthy characteristics. These include high levels of ionized gas emission (Guseva et al. 2004), previous single dish and interferometric HI observation of Pox 186 resulting in emission non-detections (Begum & Chengalur 2005), and Pox 186's classification as a Green Pea galaxy due to its circular morphology and green optical appearance via strong OIII spectral lines (McKinney et al. 2019). These two galaxies are analyzed along side Haro 11 to increase the sample size of HI non-emitters with high star formation rates to further explore this unexpected behavior.

2. OBSERVATIONS AND DATA REDUCTION

2.1. *Haro 11*

A total of 24 hours of deep spectral line observation at the 21 cm line were gathered via the VLA program 17B-287. 20 hours of this observing time were conducted in the B configuration, with the remaining 4 hours in the hybrid BnA configuration. Both the B and BnA configurations possess a high ratio of baseline length to dish area relative to other antenna configurations, making their data more sensitive to angular resolution than surface brightness. Data reduction was conducted using the Common Astronomy Software Applications (CASA) package. The source J0010-4153 was used as the phase calibrator, and the source 0137+331=3C48 was used as the primary calibrator. A second-order fit was used for continuum subtraction given the complicated morphology of background QSO sources, and a tapered clean was employed for imaging given the extreme southerly declination of the source. The first frame of the final data cube, created by imaging all datasets together and used to obtain the rms noise value (see Table 2), can be seen in Figure 5.

6

2.2. *Pox 186*

Archival VLA observations from the program AS0832 at the 21 cm line of the source POX 186 were obtained from the National Radio Astronomy Observatory (NRAO) archive. Just under three hours (176 minutes) of on-source observing time were conducted in the C configuration. This configuration possesses a lower ratio of baseline length to dish area relative to other VLA antenna configurations, making the data from this program more sensitive to surface brightness than angular resolution. Reduction for this archival dataset was conducted using CASA, with the source 1331+305 serving as the primary calibrator and the source 1351-148 serving as the phase calibrator. A second-order fit was used for continuum subtraction due to the complicated morphology of background QSO sources. The first frame of the final data cube, created via imaging all datasets together and used to obtain the rms noise value (see Table 2), can be seen in Figure 6.

2.3. *VCC 1313*

VLA observations from the program AS0832 at the 21 cm line of the source VCC 1313 were obtained from the NRAO data archive. Approximately two and a half hours (203 minutes) of on-source observing time were conducted in the C configuration. These data were reduced using CASA, with the source 1331+305 serving as the primary calibrator, and the source 1254+116 serving as the phase calibrator. A second-order fit was used for continuum subtraction due to the complicated morphology of background QSO sources, as well as the significant prominence of the galaxy NGC 4374, or M84, in the northern region of the field. The first frame of the final data cube, created by imaging all datasets together and used to obtain the rms noise value (see Table 2), can be seen in Figure 7.

3. RESULTS

3.1. *Haro 11*

3.1.1. *Emission*

After imaging together all 24 hours of VLA data for Haro 11, the result of a HI non-detection in emission is confirmed. This conclusion is supported by Figures 8, 9, 10, and 11, spectra of HI flux density as a function of velocity, acquired using apertures centered on Haro 11's α and δ (see Table 1) with respective sizes of 19" × 19", 33" × 33", 1.5' × 1.5', and 3' × 3', and beam size 17.740" × 11.450". Different aperture sizes were used to ensure that the non-detection result remained valid farther out from the galaxy's center (i.e. if the HI gas were dispersed enough, a larger aperture would result in an HI emission detection). These spectra contain solely noise, meaning there are no characteristic peaks as there would be if an emission detection were the result. The rms noise value from the final data cube is 1.43 mJy Bm^{-1}.

From this rms noise value, we are able to calculate an upper mass limit using the following equation:

$$M_{HI} = 236 \times D_L^2 \times S_{21} \times M_\odot$$

Assuming a distance of 88 Mpc (Pardy et al. 2016), and a line width of 160 km s^{-1} (Pardy et al. 2016), for a S$_{21}$ value of 0.2288 Jy km s^{-1}, the resulting 2σ upper mass limit value is 8.4 ×10^8 M$_\odot$ (see Table 2). This value is slightly larger than the HI mass limit derived by (Pardy et al. 2016) of $5.1 \pm 0.7 \times 10^8$ M$_\odot$.

3.1.2. *Absorption*

Although Haro 11's HI emission result is a non-detection, the non-continuum subtracted data produce a detection of HI in absorption, confirming the absorption detection published by MacHattie et al. (2014). The spectrum from which this conclusion arises can be seen in Figure 12, obtained using an aperture size of 40" × 40", with beam size of 18.858" × 11.779". An absorption trough can

8

be seen centered at a velocity value just above 6100 km s^{-1}. This center is shifted slightly blueward of the system's optical velocity of 6175 km s^{-1}, a shift that is qualitatively similar to that detected by (Pardy et al. 2016), but in the other direction. In other words, the velocity shift detected by (Pardy et al. 2016) was a redward one (i.e. to higher velocity).

From this absorption trough, a value for the column density of the HI gas becomes calculable. By first assuming a spin temperature of 100 K, a value within the proposed range by MacHattie et al. (2014) of 90 K $\leq T_s \leq$ 200 K, the resulting column density is 1.4×10^{21} cm^{-1}. This value is slightly smaller than the range given by MacHattie et al. (2014) of N$_{HI}$ = $(3.1\pm0.2)\times10^{21}$ to $(1.1\pm0.7)\times10^{22}$ cm^{-2}. By raising the assumed spin temperature to the value 200 K, still within the acceptable range proposed by MacHattie et al. (2014) and agreeing with the temperature suggested by Cormier et al. (2014), the column density value becomes 2.8×10^{21} cm^{-2}, a value that agrees with that proposed by MacHattie et al. (2014) within errors, and seen in Table 2.

3.2. *Pox 186*

After imaging together the archival VLA data for Pox 186, the HI non-detection result is confirmed. This conclusion is based on spectra of Pox 186's HI flux density as a function of velocity, which can be seen in Figures 13, 14, 15, and 16. The aperture sizes used to obtain these spectra are 20" × 20", 40" × 40", 1.5' × 1.5', and 3' × 3', centered on Pox 186's α and δ, with beam size 21.141" × 13.817". The same lack of peaks as was seen in Haro 11's spectra can be seen in Pox 186's, indicative of a non-detection result. The rms noise value from the final data cube is 1.0 mJy Bm^{-1}. Assuming a line width of 36.1 km s^{-1} (McKinney et al. 2019), and following the same calculation process described in section 3.1.1 for Haro 11, assuming a distance of 18.5 Mpc (Cormier et al. 2014), and S$_{21}$ value of 0.0361 Jy km s^{-1}, the resulting 2σ upper mass limit for HI in Pox 186 is 5.8 $\times10^6$ M$_{\odot}$. This can be seen in Table 2.

3.3. *VCC 1313*

After imaging together the archival VLA data for VCC 1313, an HI non-detection is the result. This arises from VCC 1313's spectra of HI flux density as a function of velocity, which can be see in Figures 17, 18, 19, and 20. These spectra were obtained using respective aperture sizes of 20" × 20", 40" × 40", 1.5' × 1.5', and 3' × 3', centered on VCC 1313's α and δ, with beam size 16.995" × 14.240". As with Pox 186 and Haro 11, these spectra exhibit no peak, indicative of a non-detection result. The rms noise obtained from the final data cube is 1.36 mJy Bm^{-1}. Assuming the same line width of 36.1 km s^{-1} as used with Pox 186 (McKinney et al. 2019), an S_{21} value of 0.0491 Jy km s^{-1}, a distance value of 16.5 Mpc (Meyer et al. 2014), and following the same methodology for calculation as described with Haro 11 in Section 3.1.1, the upper mass limit calculated for VCC 1313 is 6.3 $\times 10^6$ $M_\odot$, which can be seen in Table 2.

4. DISCUSSION

The most significant clash between the results from this capstone work and past literature relates to the high star formation rates reported for all three galaxies and the non-detection of HI in each galaxy. Since HI mass is correlated with SFR according to Teich et al. (2016), it would logically follow that galaxies with high SFRs would contain more HI gas, leading to HI emission detections. Despite this tension, there are numerous theories that may explain the origins of this enigmatic behavior. One of these theories, discussed by Rivera-Thorsen et al. (2017), deals with stellar feedback and galactic winds driving HI gas out of the host galaxy. Stellar feedback and galactic winds have been associated with the evolution of dwarf galaxies like Haro 11, Pox 186, and VCC 1313 in the past (Mashchenko et al. 2008). In a general sense, throughout the lifetime of stars, a range of outbursts of materials can impact the ISM where a significant amount of the HI gas in the galaxy is located. These outbursts, especially when caused by energetic events such as supernova explosions, push the HI gas in the ISM

10

of these galaxies great distances, with the HI's appearance akin to shells and chimneys (Ceverino & Klypin 2009). This phenomenon is especially pronounced when the HI gas is pushed perpendicularly to the plane of the galaxy, which is where the bulk of the galaxy's mass is located. Consequently, the gas travels through regions that are less dense than those located in the bulk plane of the galaxy, and therefore is able to spread from the bulk mass of the galaxy with ease. It is this outpouring of gas from the galaxy caused by these galactic winds that Rivera-Thorsen et al. (2017) suggest is one of the reasons for the non-detection of HI in Haro 11 in particular.

This same line of logic can be applied to Pox 186 and VCC 1313 as well. A paper by Corbin et al. (2006) suggests that the low metallicities of dwarf galaxies are likely due to the escape of supernova ejecta. Since Pox 186 and VCC 1313 both possess low metallicities (see Table 1), and galactic winds are associated with supernova ejecta as previously discussed, it is reasonable to think that these low metallicities are caused by galactic winds. It therefore follows that the same galactic winds causing these low metallicities could also be pushing the HI gas out of these galaxies. With this logic, the HI emission non-detections in both Pox 186 and VCC 1313 would be logical.

Another theory that exists to explain the non-detection of HI gas in these systems suggests that Haro 11 has an unusually high ratio of ionized to neutral hydrogen gas in terms of mass. This theory, explained by Bergvall & Östlin (2002), is corroborated by Pardy et al. (2016). By looking at far-IR observations, Bergvall & Östlin (2002) suggest an ionized gas mass on the order of $10 \pm 1 \times 10^8$ M$_\odot$, a value slightly greater than the upper HI limit proposed by observations made for this capstone (see Table 2). This theory is corroborated by Menacho et al. (2019), which found rich structural features in the ionized hydrogen in Haro 11, and concluded that most of the gas content of Haro 11 is indeed photoionized and hot, thereby explaining the HI non-detection result. Extending this theory to Pox 186 poses no difficulties. Results published by Guseva et al. (2004) suggest that most of the gas in Pox 186, both hydrogen and heavier elements such as helium and oxygen, is likely ionized, again

explaining the result of an HI non-detection.

A third theory that exists to explain the HI emission non-detection in these galaxies deals with tidal structure that lowers the surface brightness of the HI emission. Specifically, Östlin et al. (2015) analyzed the kinematics of Haro 11 via emission lines from ionized hydrogen, OIII, and SIII, the results from which suggest that Haro 11 is likely the result of a past merger. This merger produced atypical kinematic behaviors in the galaxy, which currently cause the HI gas in the galaxy to be more tenuous and extended in its distribution. The extended nature of the HI gas would therefore explain the non-emission result for Haro 11. Applying this same theory to Pox 186 again poses no challenges. Research published by Corbin & Vacca (2002) suggests that Pox 186 may be the result of a merger as well, although this merger may not have occured on the same size scale as Haro 11. Corbin & Vacca (2002) suggest that Pox 186's origins are a merger of two clumps of stars of subgalactic size. Nonetheless, the low surface brightness of the HI in Pox 186 could be explained by this merger theory as well, despite the smaller scale for Pox 186 than for Haro 11.

5. FUTURE WORK

Since the behavior of these three systems remains enigmatic, there are a number of areas which future research could explore. One of these is to design an interferometric program with deeper integration times and configurations with higher sensitivity to surface brightness than angular resolution. The antenna configurations used for Haro 11's data were the B and BnA configurations, both of which are more sensitive to angular resolution than surface brightness. If coupled with deeper integration times, observing these three galaxies with the previously suggested surface brightness sensitive antenna configurations could reveal more about the HI content of these systems.

Another potentially rich field for further research is looking at the distribution of ionized gas throughout the galaxies. Since an atypical ratio of ionized to neutral gas is one of the primary

12

theories for explaining the non-emitting HI in the galaxies, understanding the distribution and the kinematics of this ionized gas might uncover more details fundamental to this theory.

6. CONCLUSION

After reducing 24 hours of VLA data at the 21 cm line of the LCBG galaxy Haro 11, the results for the HI content of the system are an emission non-detection, contrary to the GBT results reported by Pardy et al. (2016). Despite an emission non-detection, an absorption detection is confirmed, re-producing the results from MacHattie et al. (2014). From both the emission non-detection and absorption detection, an upper limit on the HI mass and column density of the system become respectively calculable, the results of which can be seen in Table 2.

Haro 11 is a galaxy known to possess a high rate of star formation, and as such, the non-emission result of HI in the galaxy is unexpected. As such, two other analogous systems were brought in to study for this capstone, Pox 186 and VCC 1313. After reducing 176 and 203 respective minutes of archival 21 cm line VLA data, the result of non-detection of HI in emission stands for both galaxies. From these results, HI mass limits were calculated, the results from which can be seen in Table 2.

Given the aggressive star formation rates of all three galaxies, the above results are highly confounding. Despite this, there exist a number of theories that could potentially explain this behavior. These theories include the galaxies possessing an unusually high ratio of ionized to neutral gas, stellar feedback driving the neutral hydrogen gas out of the galaxies, and remnant atypical kinematic behaviors from past mergers. None of these theories are confirmed, but there exist possibilities for further research to explore them. For now, however, the behavior of each of these three HI non-emitting galaxies remains enigmatic.

14

7. TABLES AND FIGURES
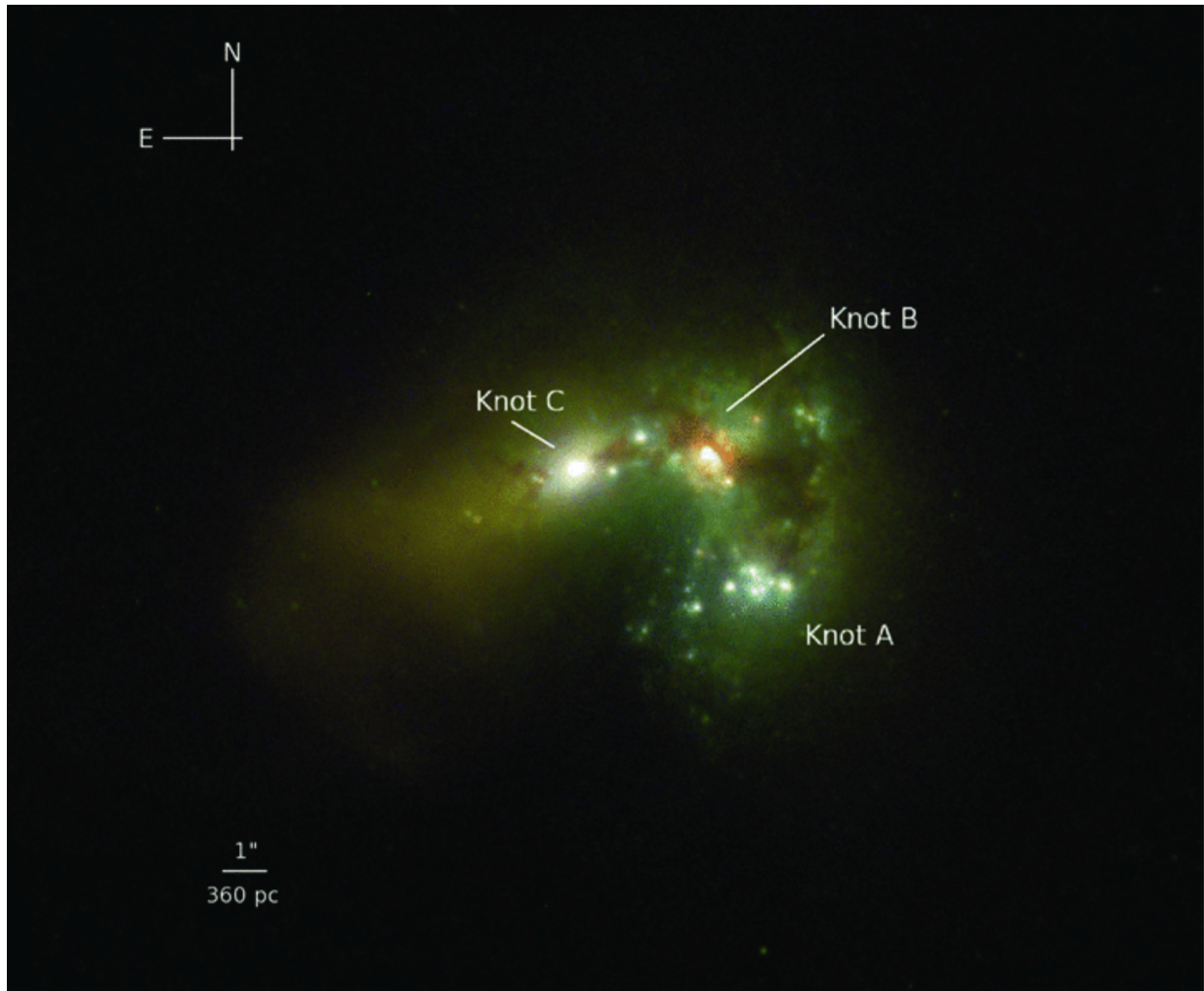
Figure 1. An optical HST image of Haro 11 from (Adamo et al. 2010). The primary star forming knots are labeled. Knots A and B exhibit Lyα absorption, while knot C exhibits Lyα emission. The galaxy shows a bean-like morphology, likely indicative of a past merger event. Note the dust lanes overlapping knot B, and lack of dust lanes overlapping knot C, an unexpected composition given the conclusion by Atek et al. (2008) that the dust content and extinction values of knots B and C are very similar.
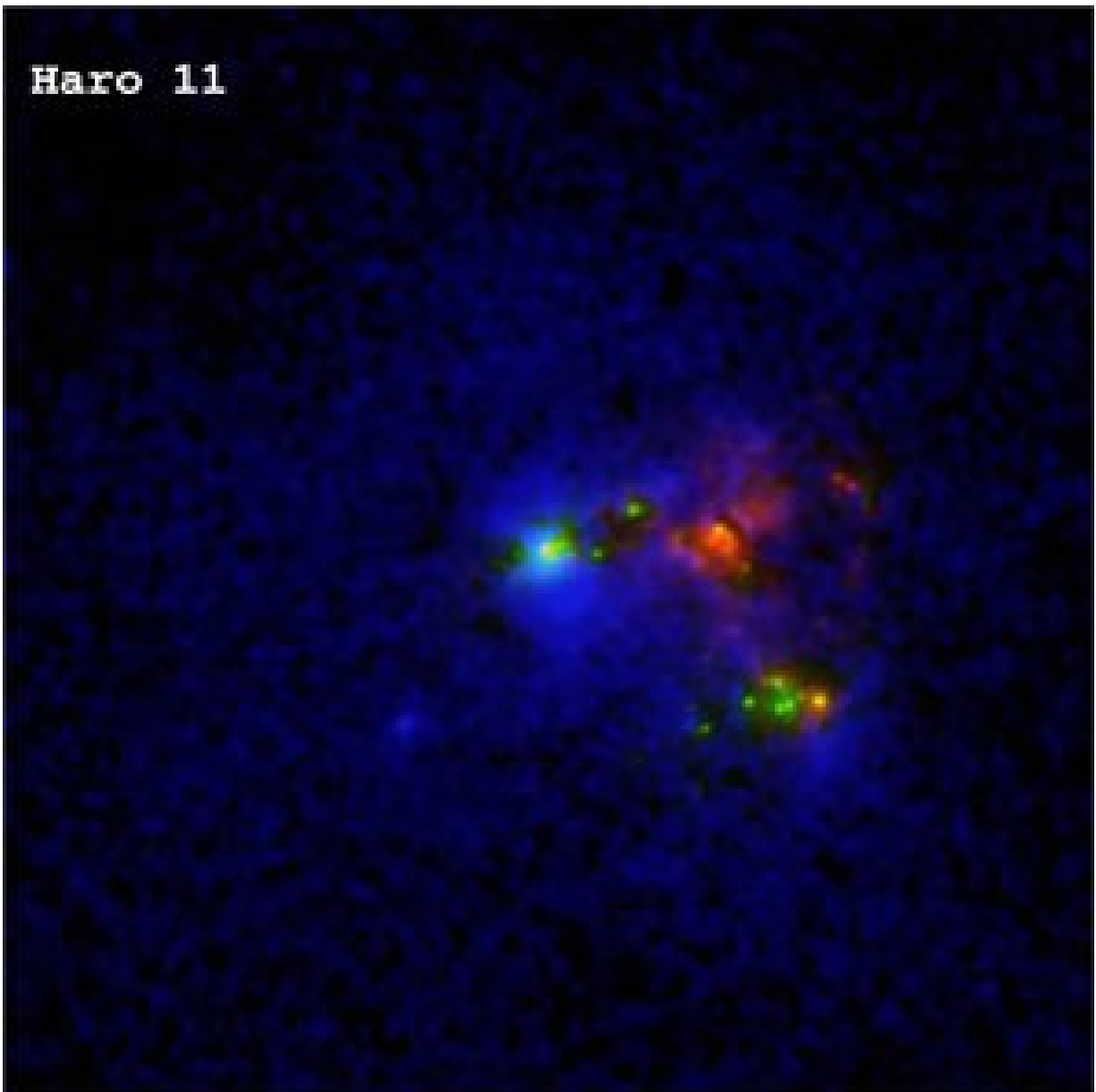
Figure 2. Haro 11 from Östlin et al. (2009). Blue corresponds to Lyα emission, red to Hα emission, and green to continuum emission at 1500 Å. Note the extended distribution of the Lyα emission far from the center of the galaxy, and the prominence of Lyα emission near knot C, and lack of prominence near knots A and B.

16
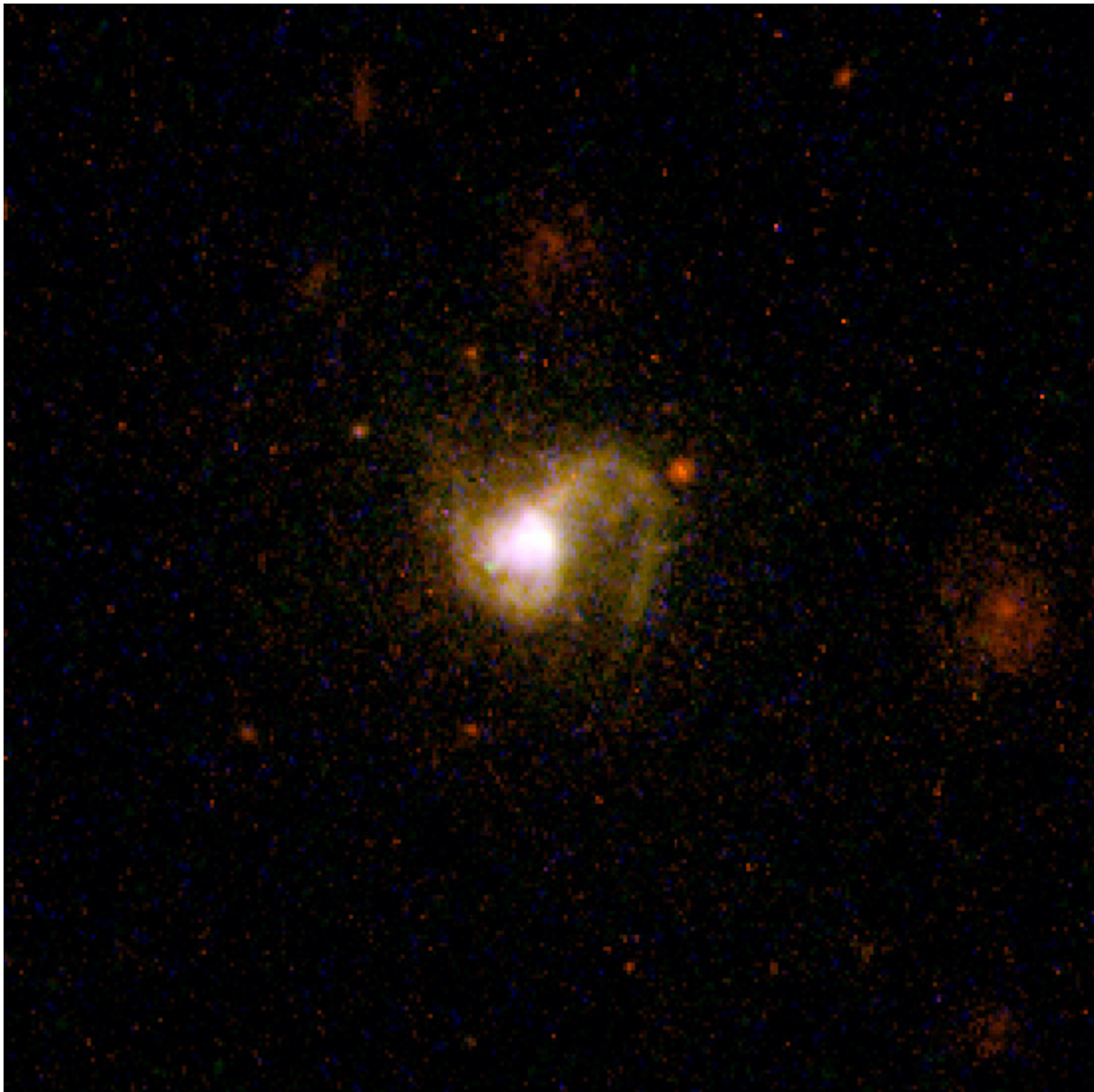
Figure 3. An archival optical HST image of Pox 186. The three broadband filters used correspond to wavelengths of 336 nm, 555 nm, and 814 nm, labeled ultraviolet (U), optical (V), and infrared (I) respectively. Note the circular morphology of this source, corresponding to its classification as a Green Pea galaxy.

Figure 4. An archival optical HST image of VCC 1313. Red corresponds to the narrowband filter F187N, blue to the narrowband filter F190N, and green to the broadband filter F160W.

18
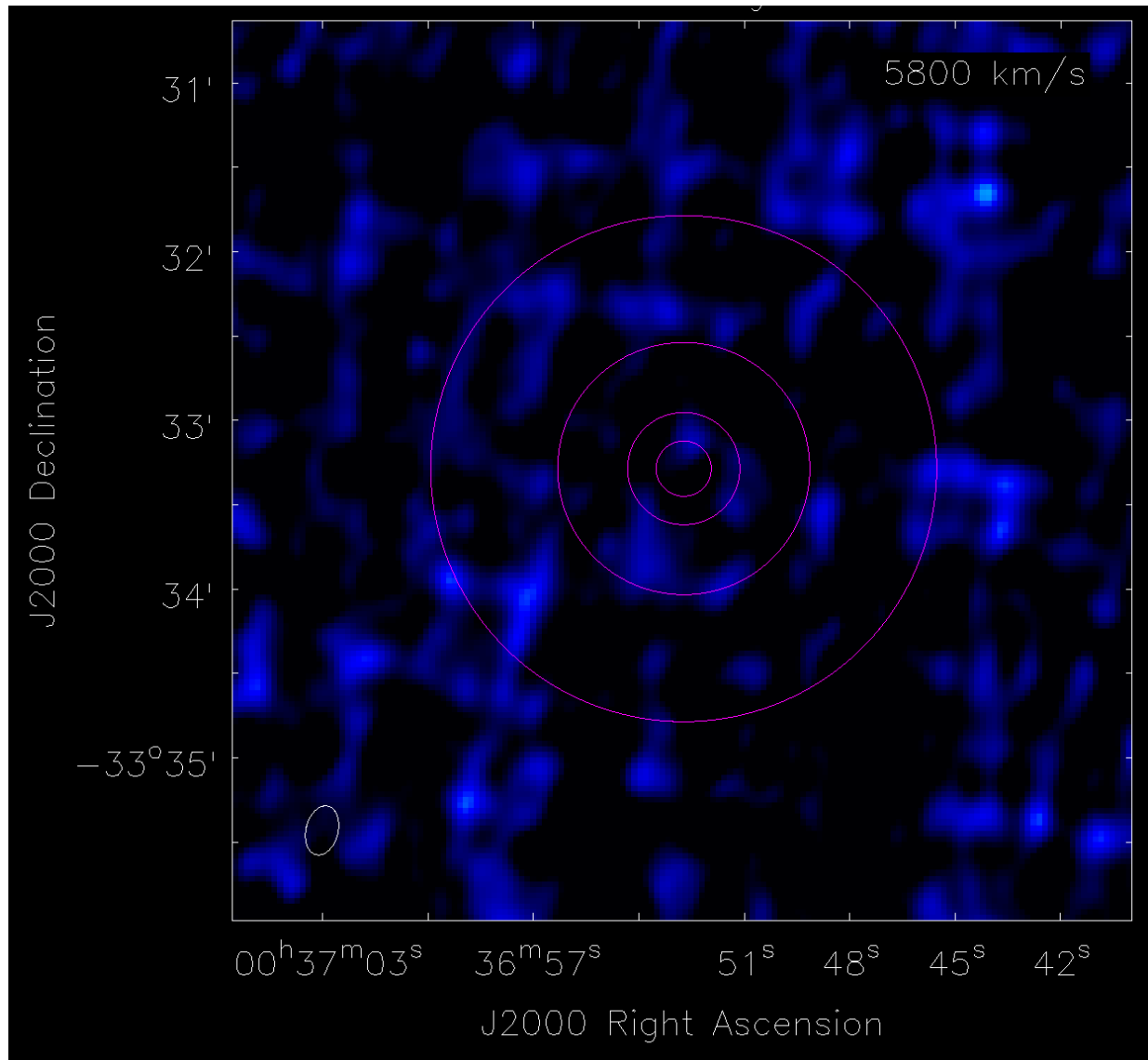
Figure 5. The first frame of the final data cube containing all 24 hours of 21 cm line VLA data of Haro 11. The magenta annuli correspond to the apertures used to obtain the emission non-detection spectra seen in Figures 8, 9, 10, and 11, with respective dimensions of 19" × 19", 33" × 33", 1.5' × 1.5', and 3' × 3'. The beam size for this data cube is 17.740" × 11.450".
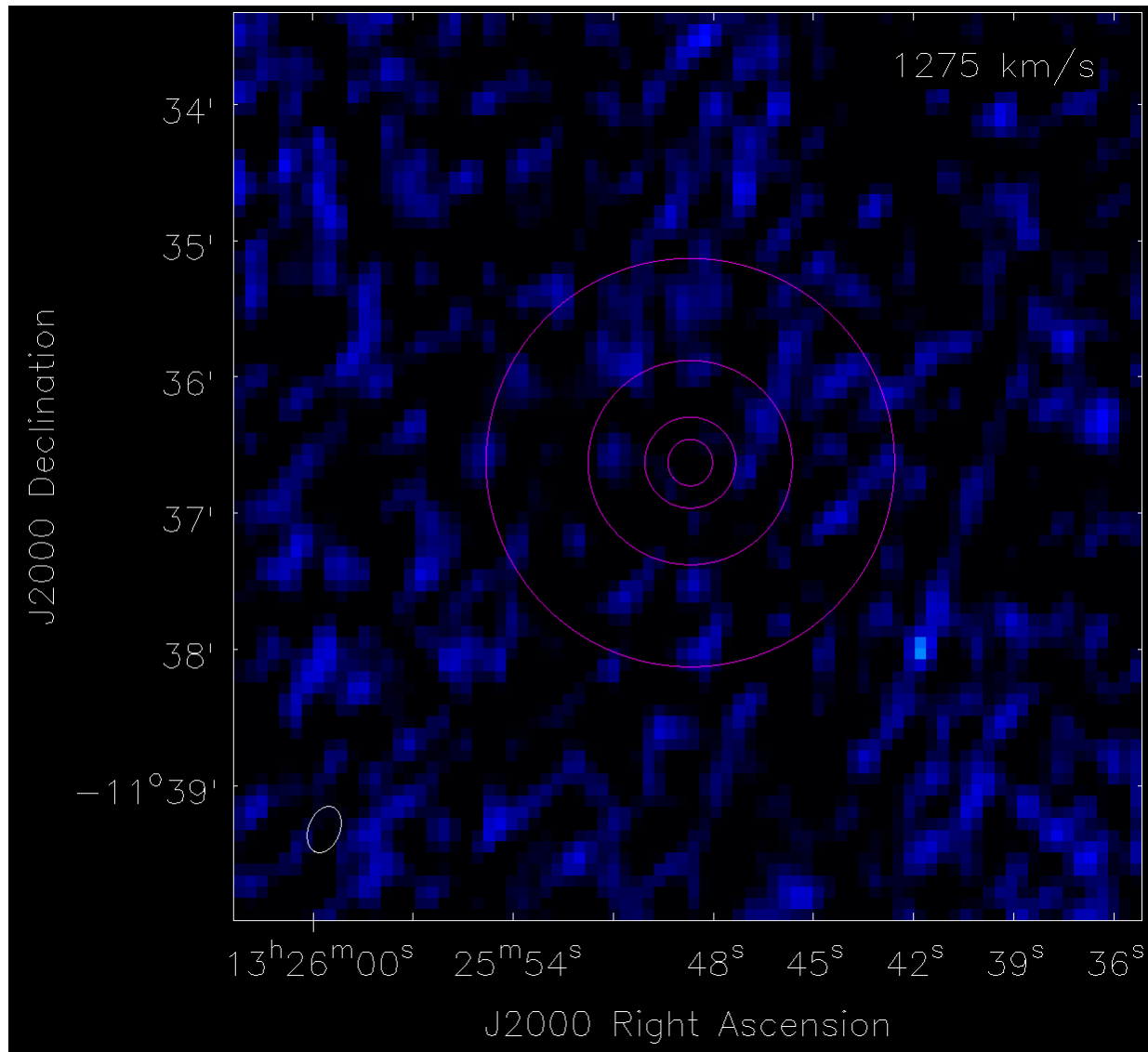
Figure 6. The first frame of the final data cube containing all 176 minutes of archival 21 cm line VLA data of Pox 186. The magenta annuli correspond to the apertures used to obtain the emission non-detection spectra seen in Figures 13, 14 15, and 16, with respective dimensions of 20" × 20", 40" × 40", 1.5' × 1.5', and 3' × 3'. The beam size for this data cube is 21.141" × 13.817".

20
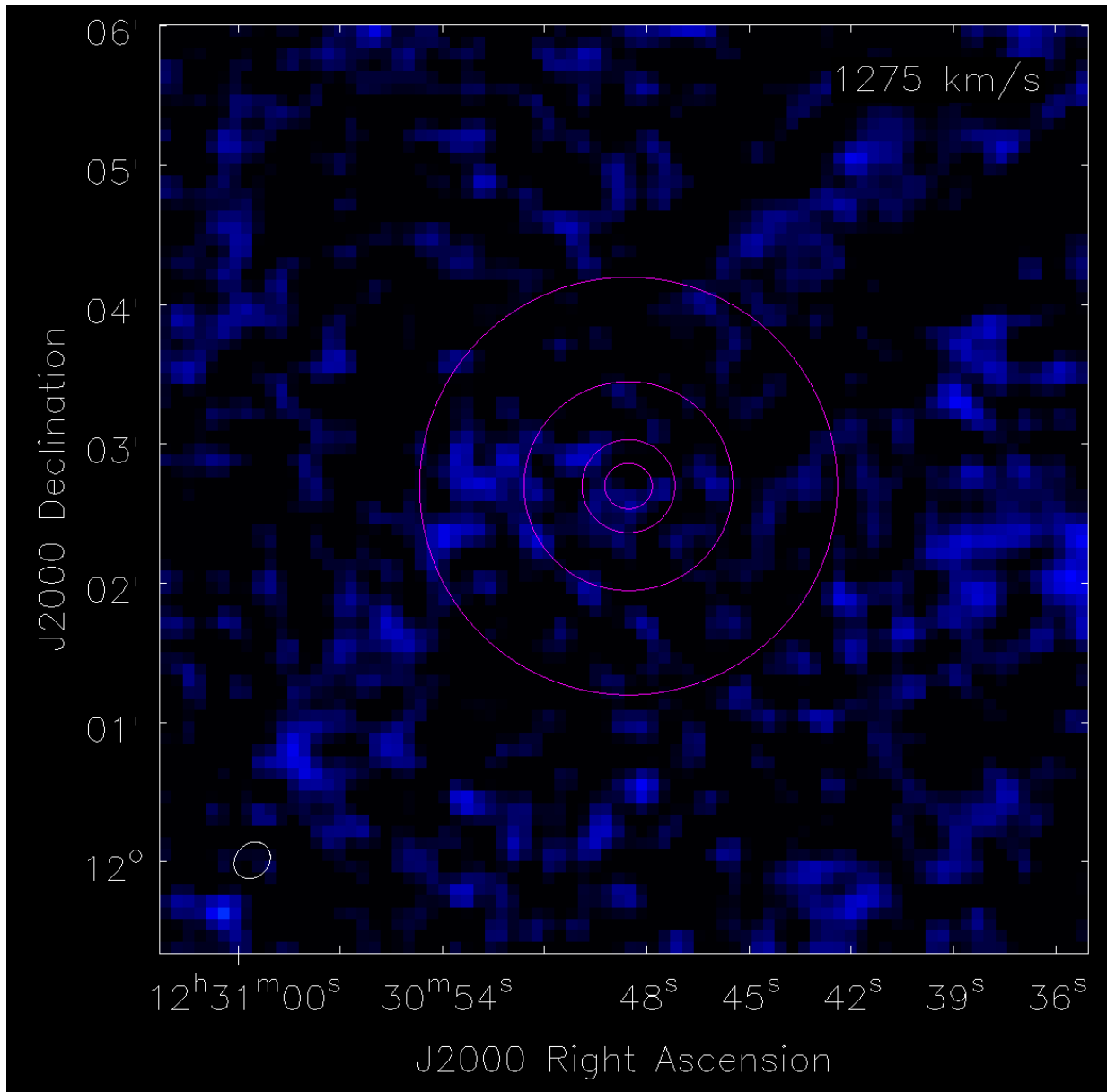
Figure 7. The first frame of the final data cube containing all 203 minutes of archival 21 cm line VLA data of VCC 1313. The magenta annuli correspond to the apertures used to obtain the emission non-detection spectra seen in Figures 17, 18, 19, and 20, with respective dimensions of 20" × 20", 40" × 40", 1.5' × 1.5', and 3' × 3'. The beam size for this data cube is 21.141" × 13.817".
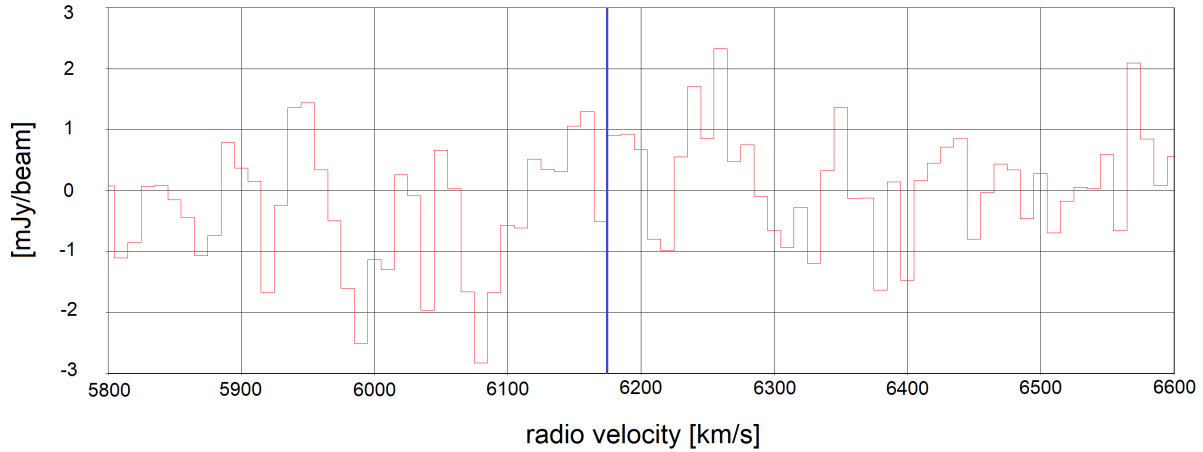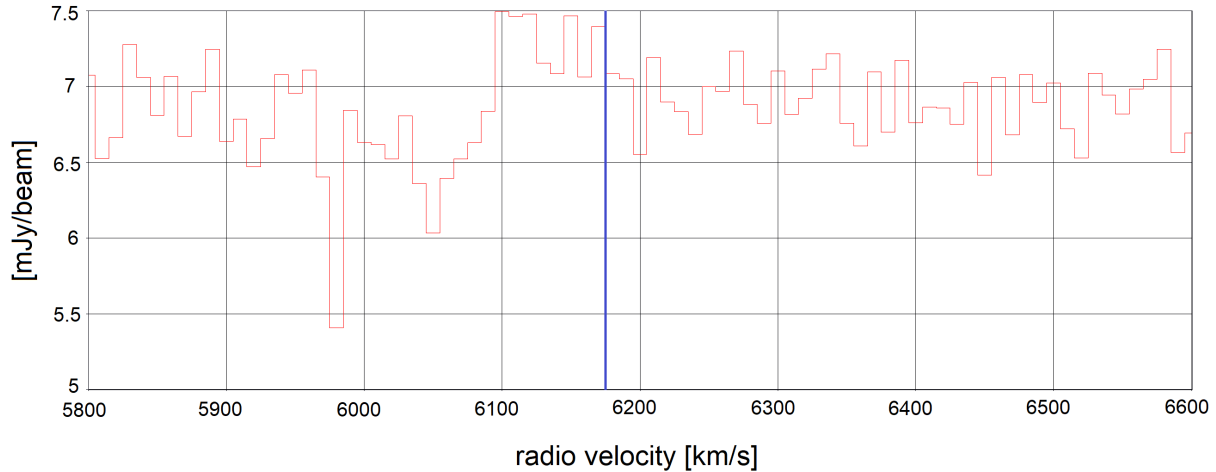
Figure 8. Spectrum of continuum subtracted flux density as a function of velocity of Haro 11 obtained using the smallest aperture with dimensions 19" × 19", centered on Haro 11's α and δ. The system's optical velocity of 6175 km s^{-1} is indicated by the solid vertical blue line. Note the lack of peak in this spectrum, indicative of an HI non-detection result.
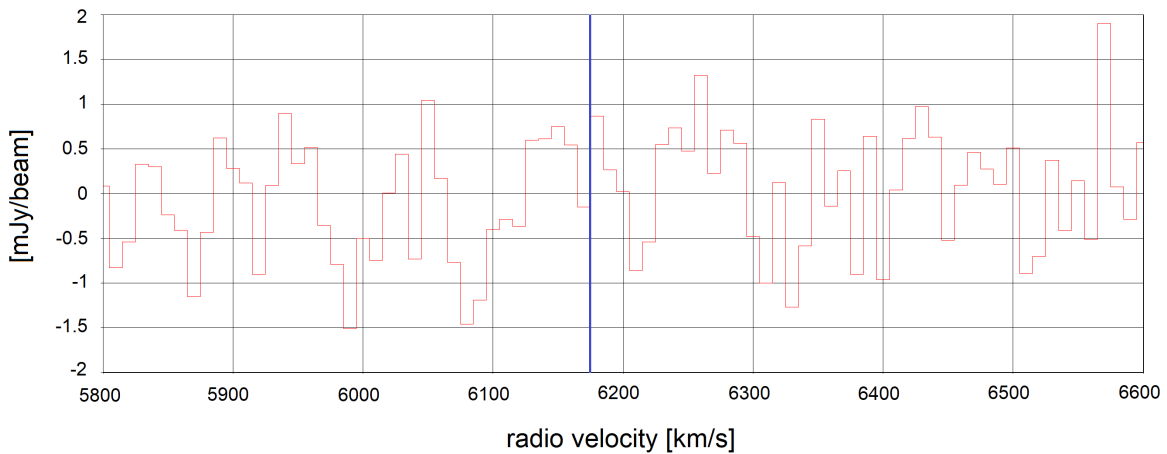
Figure 9. Spectrum of continuum subtracted flux density as a function of velocity of Haro 11 obtained using the second smallest aperture with dimensions 33" × 33", centered on Haro 11's α and δ. The system's optical velocity of 6175 km s^{-1} is indicated by the solid vertical blue line. Note the lack of peak in the spectrum, further indicative of an HI non-detection result.
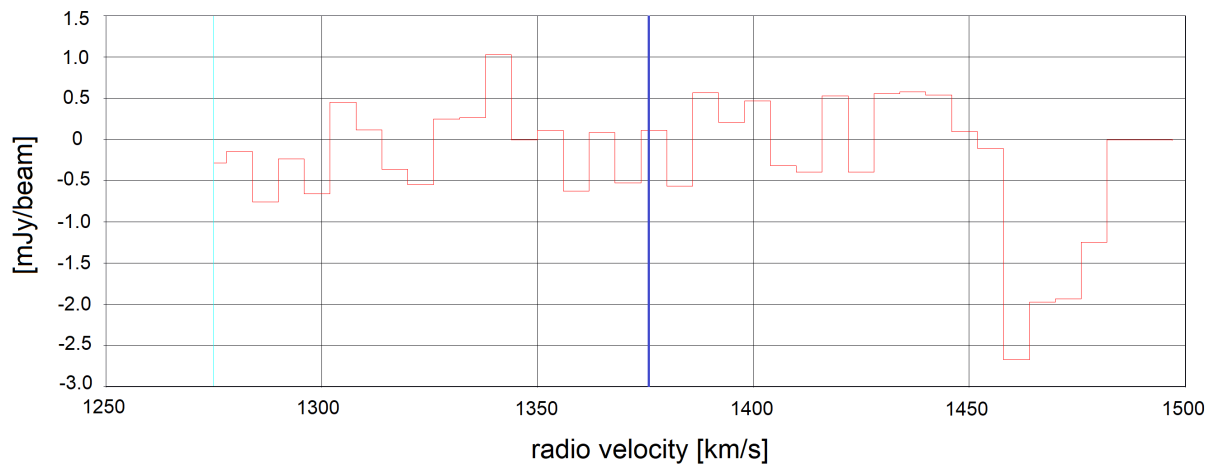
22
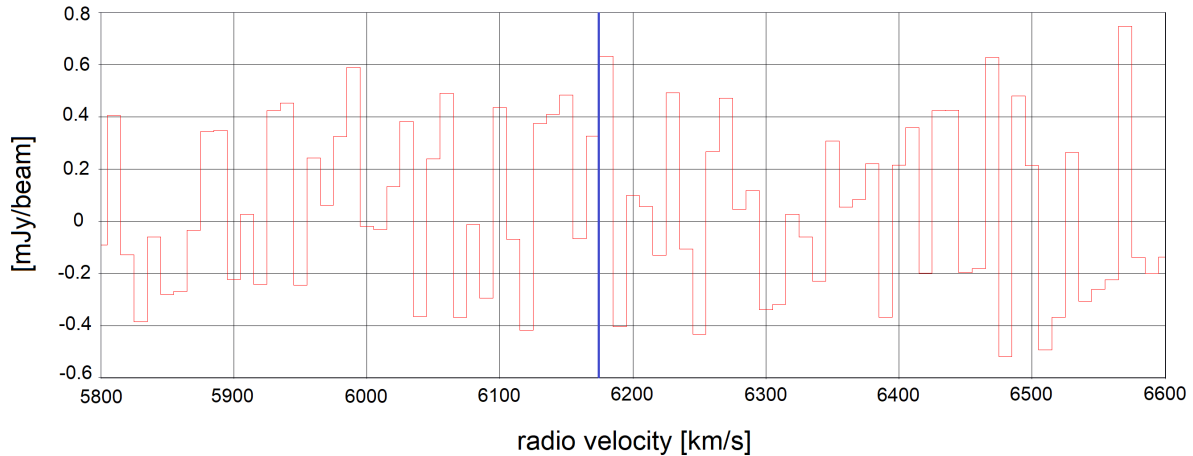
Figure 10. Spectrum of continuum subtracted flux density as a function of velocity of Haro 11 obtained using the second largest aperture with dimensions 1.5' × 1.5', centered on Haro 11's α and δ. The system's optical velocity of 6175 km s^{-1} is indicated by the solid vertical blue line. Note the lack of peak in the spectrum, further indicative of an HI non-detection result.
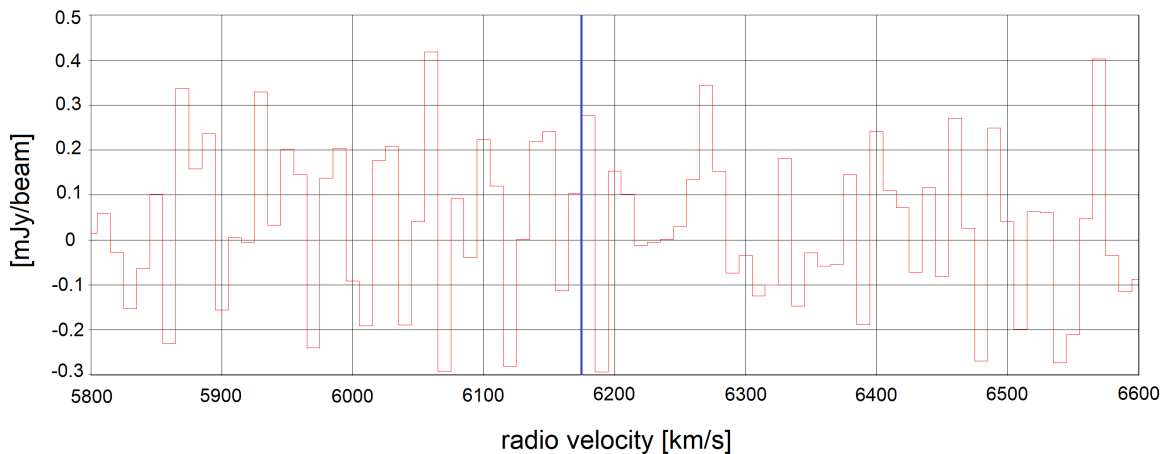
Figure 11. Spectrum of continuum subtracted flux density as a function of velocity of Haro 11 obtained using the largest aperture with dimensions 3' × 3', centered on Haro 11's α and δ. The system's optical velocity of 6175 km s^{-1} is indicated by the solid vertical blue line. Note the lack of peak in the spectrum, further indicative of an Hi non-detection result.
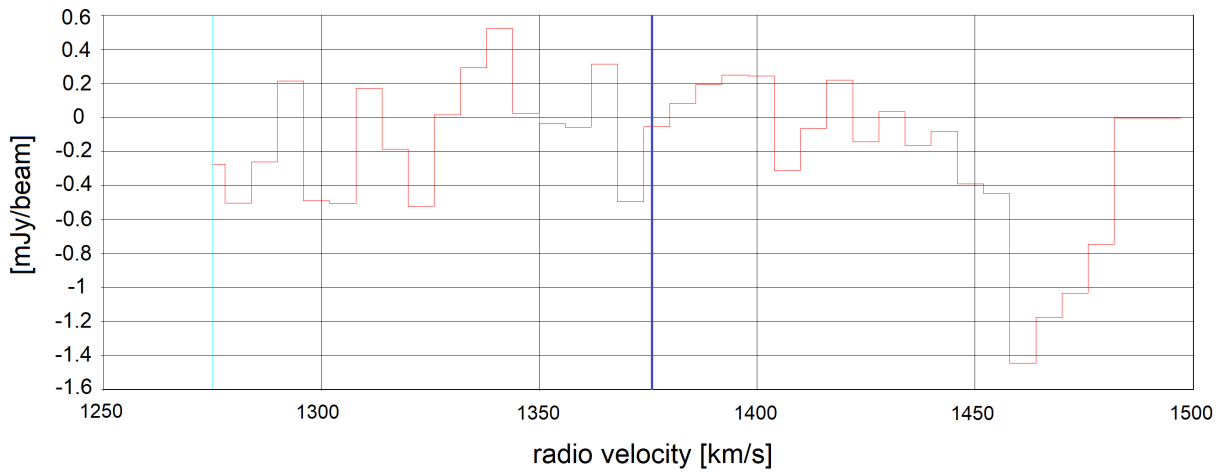
Figure 12. Spectrum of non-continuum subtracted flux density as a function of velocity of Haro 11 obtained using an aperture with dimensions 40" × 40", centered on the system's α and δ. The system's optical velocity of 6175 km s^{-1} is indicated by the solid vertical blue line. Notice the absorption trough centered at a value just greater than 6100 km s^{-1}, indicative of the HI absorption detection (i.e. Haro 11's HI absorbing against its own background continuum). Notice additionally the blueward (i.e. to a lower velocity) shift of the center of the absorption trough from the system's optical velocity. This shift is similar in nature to that detected by Pardy et al. (2016), though in the opposite direction.
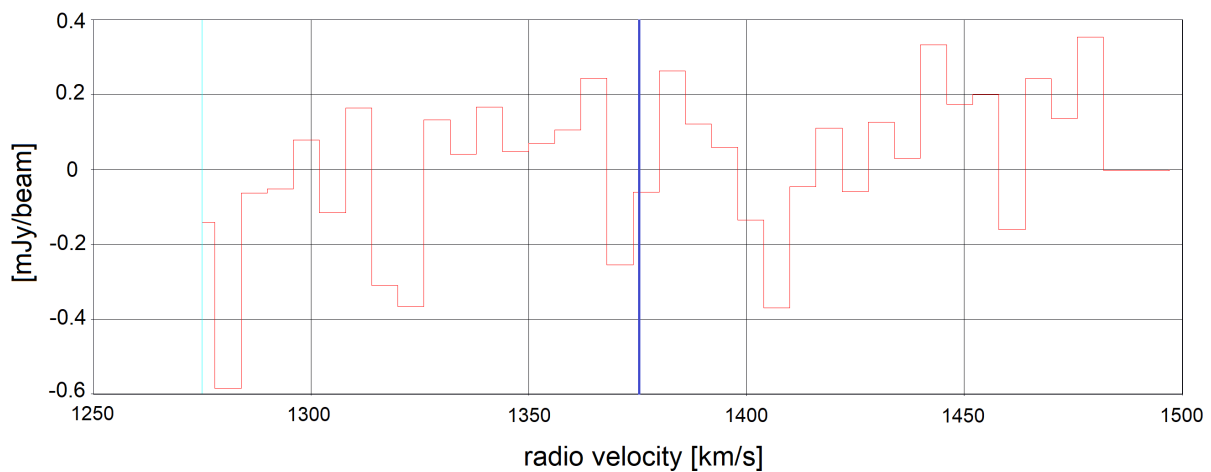

Figure 13. Spectrum of continuum subtracted flux density as a function of velocity of Pox 186 obtained using the smallest aperture with dimensions 20" × 20", centered on Pox 186's α and δ. The system's optical velocity of 1375 km s^{-1} is indicated by the solid vertical blue line. Note the lack of peak in this spectrum, indicative of an HI non-detection result.
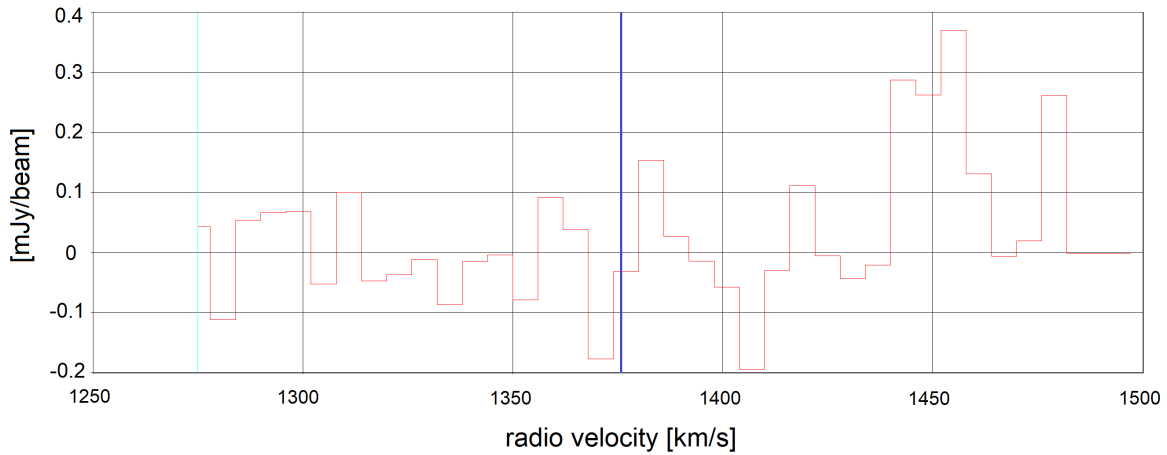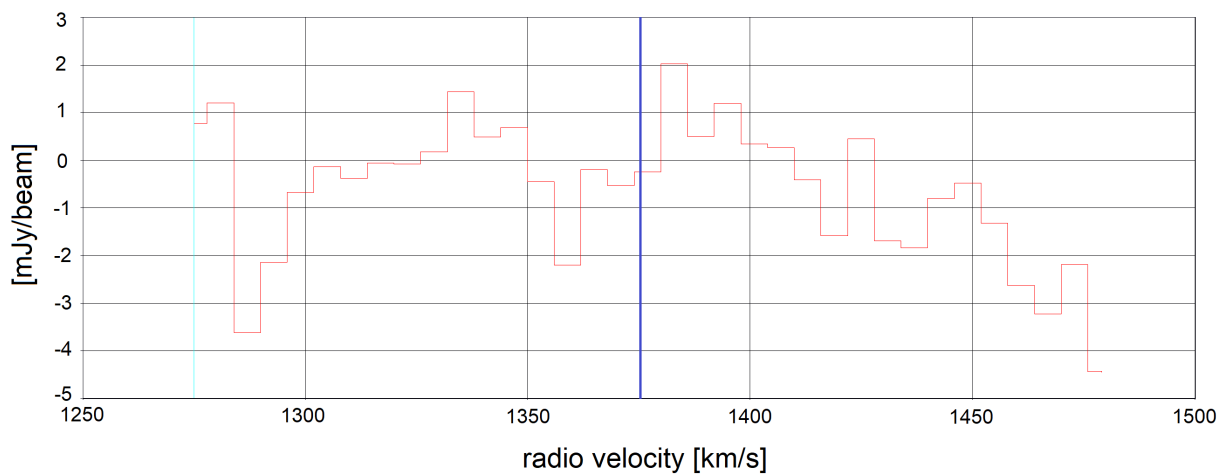
24

Figure 14. Spectrum of continuum subtracted flux density as a function of velocity of Pox 186 obtained using the second smallest aperture with dimensions 40" × 40", centered on Pox 186's α and δ. The system's optical velocity of 1375 km s^{-1} is indicated by the solid vertical blue line. Note the lack of peak in this spectrum, further indicative of an HI non-detection result.
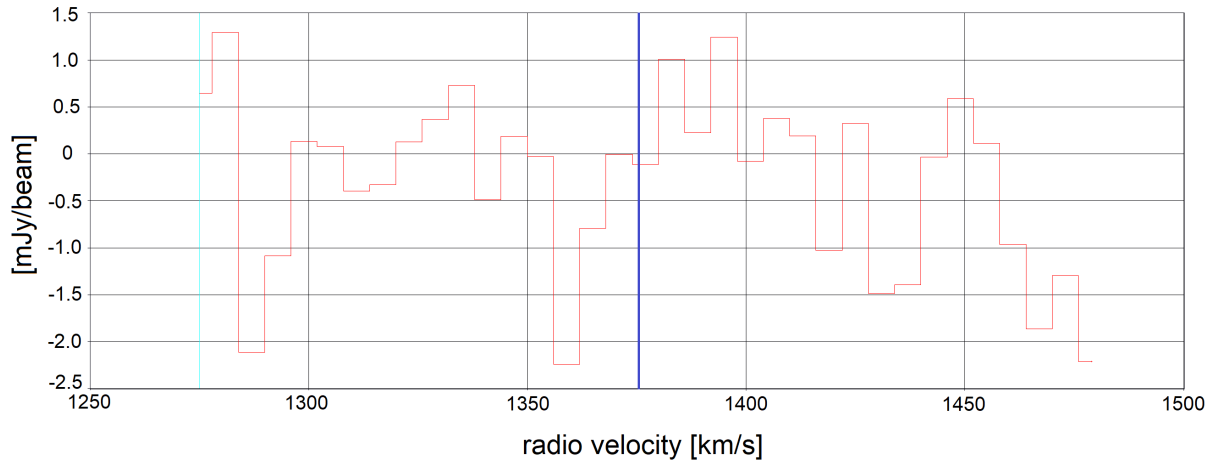

Figure 15. Spectrum of continuum subtracted flux density as a function of velocity of Pox 186 obtained using the second largest aperture with dimensions 1.5' × 1.5', centered on Pox 186's α and δ. The system's optical velocity of 1375 km s^{-1} is indicated by the solid vertical blue line. Note the lack of peak in this spectrum, further indicative of an HI non-detection result.
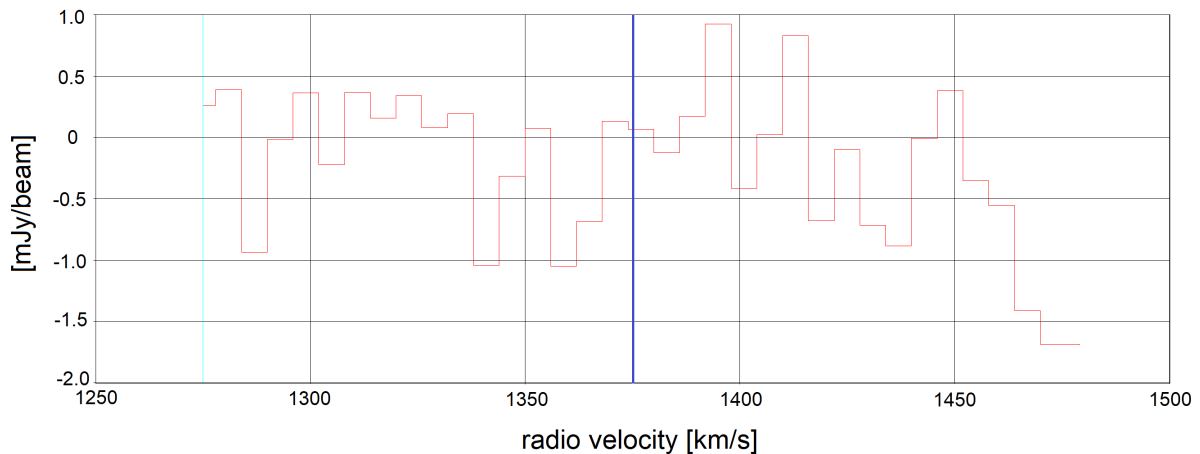
Figure 16. Spectrum of continuum subtracted flux density as a function of velocity of Pox 186 obtained using the largest aperture with dimensions 3' × 3', centered on Pox 186's α and δ. The system's optical velocity of 1375 km s^{-1} is indicated by the solid vertical blue line. Note the lack of peak in this spectrum, further indicative of an HI non-detection result.
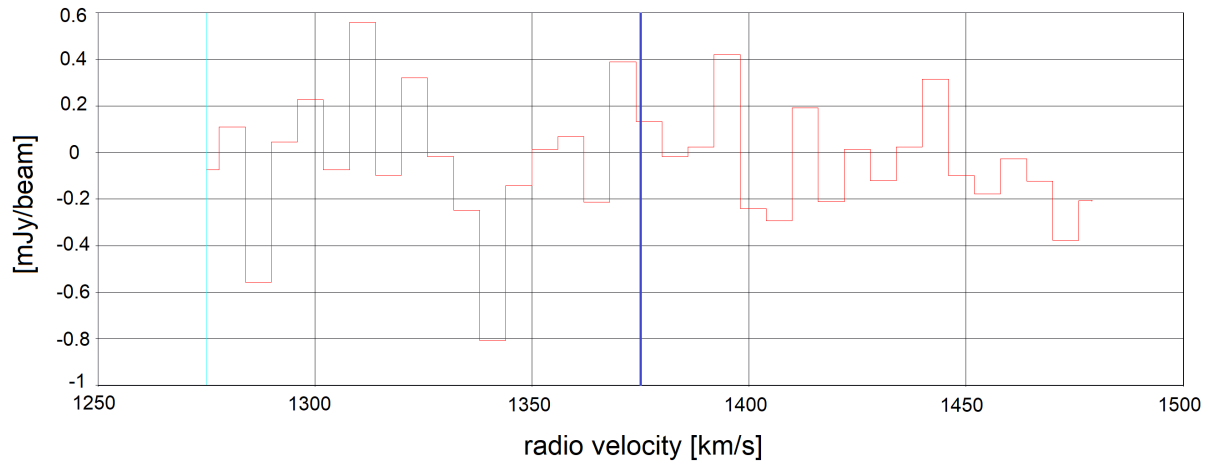

Figure 17. Spectrum of continuum subtracted flux density as a function of velocity of VCC 1313 obtained using the smallest aperture with dimensions 20" × 20", centered on VCC 1313's α and δ. The system's optical velocity of 1375 km s^{-1} is indicated by the solid vertical blue line. Note the lack of peak in this spectrum, indicative of an HI non-detection result.

26

Figure 18. Spectrum of continuum subtracted flux density as a function of velocity of VCC 1313 obtained using the second smallest aperture with dimensions 40" × 40", centered on VCC 1313's α and δ. The system's optical velocity of 1375 km s^{-1} is indicated by the solid vertical blue line. Note the lack of peak in this spectrum, further indicative of an HI non-detection result.


Figure 19. Spectrum of continuum subtracted flux density as a function of velocity of VCC 1313 obtained using the second largest aperture with dimensions 1.5' × 1.5', centered on VCC 1313's α and δ. The system's optical velocity of 1375 km s^{-1} is indicated by the solid vertical blue line. Note the lack of peak in this spectrum, further indicative of an HI non-detection result.

Figure 20. Spectrum of continuum subtracted flux density as a function of velocity of VCC 1313 obtained using the largest aperture with dimensions 3' × 3', centered on VCC 1313's α and δ. The system's optical velocity of 1375 km s^{-1} is indicated by the solid vertical blue line. Note the lack of peak in this spectrum, further indicative of an HI non-detection result.
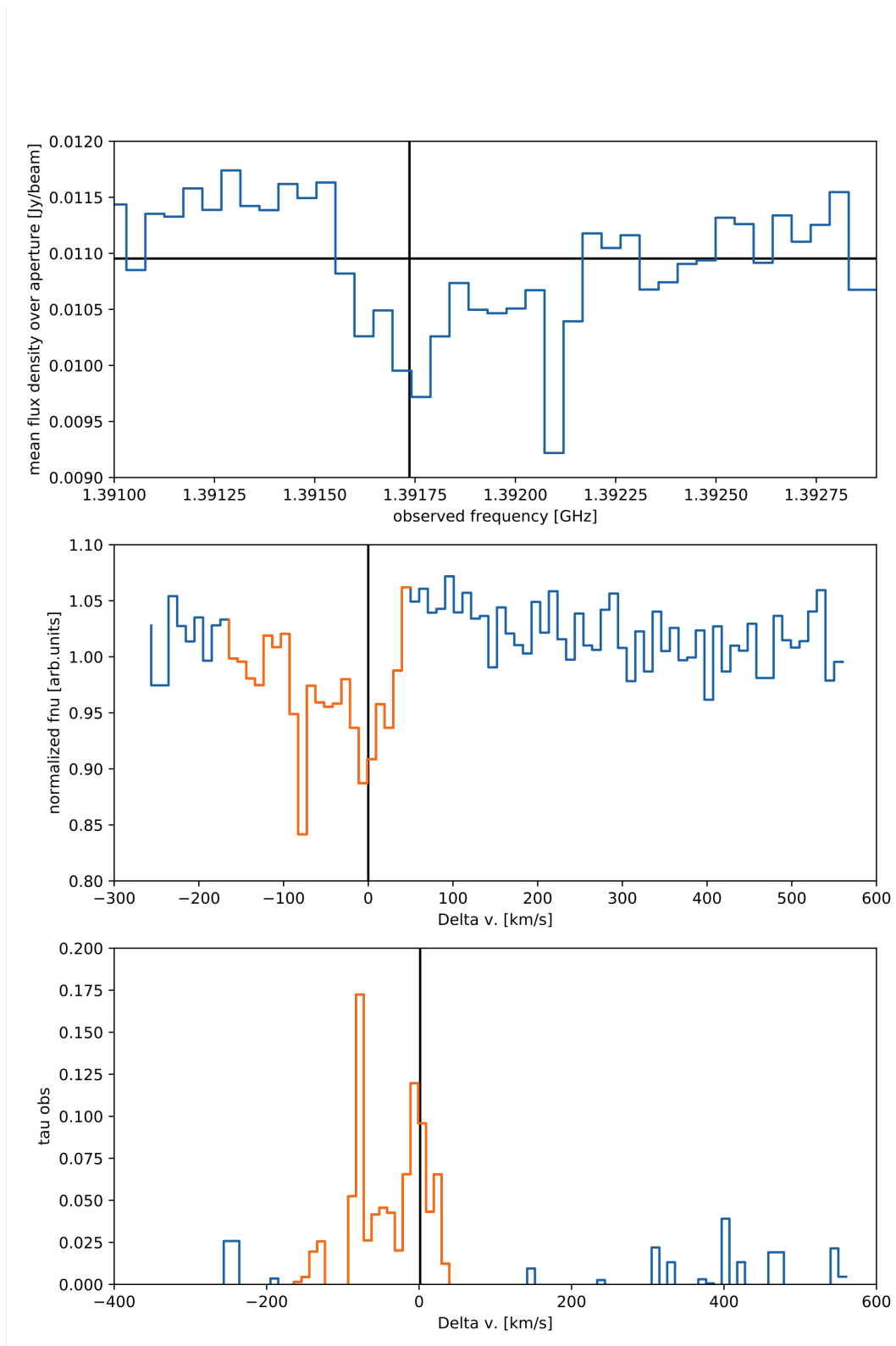
Figure 21. Panel 1: A re-production of the absorption spectrum seen in Figure 12. Panel 2: A normalized version of the first panel, allowing examination of the quality of the local baseline fit. Panel 3: Optical depth of the fitted HI profile used to calculate the HI column density.

	Haro 11	Pox 186	VCC 1313
α, δ	00h36m52.70s, -33d33m17.0s	13h25m48.66s, -11d36m37.78s	12h30m48.52s, +12d02m42.06s
v_{OPT}	6180 km s^{-1}	1480 $\pm$ 22 km s^{-1}	1254 $\pm$ 9 km s^{-1}
SFR	24 M$_\odot$ yr^{-1}	log(SFR/M$_\odot$) = -8.3	N/A
Distance	88 Mpc	18.5 Mpc	16.5 Mpc
Metallicty	8.2	7.76 $\pm$0.02	7.64 $\pm$0.07
M$_B$	-21.62 $\pm$0.51	-14.27 $\pm$0.50	-14.20 $\pm$0.03

Table 1. A table summarizing significant values of Haro 11, Pox 186, and VCC 1313. Row one gives the J2000 Right Ascension (R.A., α) and Declination (Dec., δ). Row two gives the optical velocity [km s^{-1}]. Row three gives the star formation rate (SFR) [M$_\odot$ yr^{-1}]. Row four gives the distance. Row five gives the metallicity. Row six gives the visible bolometric magnitude [mag].

30

	Rms noise [mJy Bm^{-1}]	HI upper limit [10^7 M$_\odot$]	Column density [10^{21} cm^{-1}]
Haro 11	1.43	84	2.8
Pox 186	1.0	0.58	–
VCC 1313	1.36	0.63	–

Table 2. A table summarizing the values calculated in this capstone, including upper HI mass limits and column density, calculated for the three galaxies Haro 11, Pox 186, and VCC 1313.

REFERENCES

Adamo, A., Östlin, G., Zackrisson, E., et al. 2010, MNRAS, 407, 870

Amorìn, R. O., Aguerri, J. A. L., Cairòs, L. M., Caon, N., & Muñoz-Tuñòn, C. 2007, in IAU Symposium, Vol. 235, Galaxy Evolution across the Hubble Time, ed. F. Combes & J. Palouš, 300-300

Atek, H., Kunth, D., Hayes, M., Östlin, G., & Mas-Hesse, J. M. 2008, AA, 488, 491

Begum, A., & Chengular, J. N. 2005, MNRAS, 362, 609

Bergvall, N., Leitet, E., Zackrisson, E., & Marquart, T. 2013, AA, 554, A38

Bergvall, N., Masegosa, J., Östlin, G., & Cernicharo, J. 2000, AA, 359, 41

Bergvall, N., & Östlin, G. 2002. AA, 390, 891

Bergvall, N., Zackrisson, E., Andersson, B.-G., et al. 2006, A&A, 448, 513

Binggeli, B., Popescu, C. C., & Tammann, G. A. 1993, Astronomy and Astrophysics Supplement Series, 98, 275

Cannon, J. M., Skillman, E. D., Kunth, D., et al. 2004, ApJ, 608, 768

Ceverino, D., & Klypin, A. 2009, ApJ, 695, 292

Corbin, M. R., & Vacca, W. D. 2002, ApJ, 581, 1039

Corbin, M. R., Vacca, W. D., Cid Fernandes, R., et al. 2006, ApJ, 651, 861

Cormier, D., Madden, S. C., Lebouteiller, V., et al. 2014, AA, 564, A121

Cowie, L. L., & Hu, E. M. 1998, AJ, 115, 1319

Field, G. B. 1959, ApJ, 129, 525

Garland, C. A., Pisano, D. J., Williams, J. P., Guzmàn, R., & Castander, F. J. 2004, ApJ, 615, 689

Guseva, N. G., Izotov, Y. I., Fricke, K. J., Henkel, C. 2012, A&A, 541, A115

Guseva, N. G., Papaderos, P., Izotov, Y. I., Noeske, K. G., & Fricke, K. J. 2004, A&A, 421, 519

Hayes, M., Östlin, G., Atek, H., et al. 2007, MNRAS, 382, 1465

Hayes, M., Östlin, G., Schaerer, D., et al. 2010, Nature, 464, 562

Huang, S., Haynes, M. P., Giovanelli, R., et al. 2014, ApJ, 793, 40

Kinman, T. D., & Davidson, K. 1981, ApJ, 243, 127

Kunth, D., Maurogordato, S., & Vigroux, L. 1988, A&A, 204, 10

Lauberts, A., & Valentijn, E. A. 1989, The surface photometry catalogue of the ESO-Uppsala galaxies

Leitet, E., Bergvall, N., Hayes, M., Linnè, S., & Zackrisson, E. 2013, A&A, 553, A106

Leitherer, C., Hernandez, S., Lee, J. C., & Oey, M. S. 2016, ApJ, 823, 64

MacHattie, J. A., Irwin, J. A., Madden, S. C., Cormier, D., & Rèmy-Ruyer, A. 2014, MNRAS, 483, L66

Mashchenko, S., Wadsley, J., & Couchman, H. M. P. 2008, Science, 319, 174

McKinney, J. H., Jaskot, A. E., Oey, M. S., et al. 2019, ApJ, 874, 52

Menacho, V., et al. 2019, in-progress

Meyer, H. T., Lisker, T., Janz, J., & Papaderos, P. 2014, A&A, 562, A49

Östlin, G., Amram, P., Bergvall, N., et al. 2001, A&A, 374, 800

Östlin, G., Hayes, M., Kunth, D., et al. 2009, AJ, 138, 923

Östlin, G., Marquart, T., Cumming, R. J., et al. 2015, A&A, 583, A55

Ouchi, M., Ono, Y., Egami, E., et al. 2009, ApJ, 696, 1164

Pardy, S. A., Cannon, J. M., Östlin, G., Hayes, M., & Bergvall, N. 2016, AJ, 152, 178

Rivera-Thorsen, T. E., Östlin, G., Hayes, M., & Puschnig, J. 2017, ApJ, 837, 29

Teich, Y. G., McNichols, A. T., Nims, E., et al. 2016, ApJ, 832, 85

Thuan, T. X., & Martin, G. E. 1981, ApJ, 247, 823